Front. Earth Sci. 2021, 15(2): 189–201
https://doi.org/10.1007/s11707-021-0889-6

RESEARCH ARTICLE

Nano- to micro-pore characterization by synchrotron radiation SAXS and nano-CT for bituminous coals

Yixin ZHAO (✉)[1,2], Chujian HAN[2], Yingfeng SUN[3,4], Nima Noraei DANESH[1,2], Tong LIU[1,2], Yirui GAO[1,2]

1 Beijing Key Laboratory for Precise Mining of Intergrown Energy and Resources, China University of Mining and Technology (Beijing), Beijing 100083, China
2 School of Energy and Mining Engineering, China University of Mining and Technology (Beijing), Beijing 100083, China
3 School of Civil and Resource Engineering, University of Science and Technology Beijing, Beijing 100083, China
4 Key Laboratory of Deep Earth Science and Engineering (Ministry of Education), Sichuan University, Chengdu 610065, China

Abstract Considering the complementarity of synchrotron radiation SAXS and nano-CT in the pore structure detection range, synchrotron radiation SAXS and nano-CT methods were combined to characterize the nano- to micro-pore structure of two bituminous coal samples. In mesopores, the pore size distribution curves exhibit unimodal distribution and the average pore diameters are similar due to the affinity of metamorphic grades of the two samples. In macropores, the sample with higher mineral matter content, especially clay mineral content, has a much higher number of pores. The fractal dimensions representing the pore surface irregularity and the pore structure heterogeneity were also characterized by synchrotron radiation SAXS and nano-CT. The fractal dimensions estimated by both methods for different pore sizes show consistency and the sample with smaller average pore diameters has a more complex pore structure within the full tested range.

Keywords synchrotron radiation, SAXS, nano-CT, pore size distribution, fractal, coal

1 Introduction

Coal is a dual-porosity organic rock with complicated pore structure from nano to micro scales. The International Union of Pure and Applied Chemistry (IUPAC) has classified the pores into three categories: micropores (<2 nm), mesopores (2 nm–50 nm), and macropores (>50 nm) (Rouquerol et al., 1994). Both radiation methods and fluid intrusion methods are commonly used for pore characterization. Radiation methods include scanning electron microscopy (SEM), transmission electron microscopy (TEM), small-angle X-ray scattering (SAXS), small-angle neutron scattering (SANS), nuclear magnetic resonance (NMR), and CT scanning methods (Suggate and Dickinson, 2004; Mastalerz et al., 2012; Giffin et al., 2013; Zhao et al., 2014; Li et al., 2017; Zhao et al., 2018; Zheng et al., 2018). Fluid intrusion methods include mercury injection porosimetry (MIP), and nitrogen and carbon dioxide low-pressure gas adsorption (LPGA) (Rootare and Prenzlow, 1967; Rodrigues and Lemos de Sousa, 2002; Mahamud and Novo, 2008). Different methods have unique features and applications. Due to the complexity of pore size distribution (PSD) of coal, it is hard to characterize the coal pore structure by a single method to cover a full range of pore sizes.

Synchrotron radiation SAXS serving as a nondestructive pore structure measurement technique has been extensively employed to characterize the pore structure of substances with electron density nonuniform regions (Mares et al., 2009; Luo et al., 2016; Syed et al., 2018), and it can simultaneously measure the interconnected pores and isolated pores within its probing range (Pan et al., 2016; Zhao et al., 2019). Through SAXS measurement, scattering curve, PSD, specific surface area (SSA), and fractal dimension of coals can be quantitatively characterized (Bale and Schmidt, 1984; Benedetti and Ciccariello, 1996; Radlinski et al., 2004; Mares et al., 2009).

Synchrotron radiation nano-CT is also a powerful tool to reconstruct the 2D and 3D pore structure of porous medium in nanoscale. This offers a unique opportunity to study fluid transport in a 3D-constructed structure of coal. Sun et al. (2008a) proposed an image processing method for shale nanopore structure based on synchrotron radiation nano-CT and a novel method for quantifying

Received September 27, 2020; accepted March 1, 2021

E-mails: zhaoyx@cumtb.edu.cn; zhaoyixin_cumtb@hotmail.com

the pore structure heterogeneity and anisotropy of shale. Wang et al. (2019) combined micro-CT and synchrotron radiation nano-CT methods to achieve the characterization of shale pore structure from 10 nm to 3.2 μm. In terms of the application of synchrotron radiation nano-CT in coal, we have carried out some previous studies on coal. The 3D models of the coal pore structure based on nano-CT images were reconstructed, and between-class variance maximization (BCVM) algorithm was used to determine the segmentation threshold of the pore structure. PSD, volume fraction, the heterogeneity and anisotropy of coal pore structure have been reported earlier by some researchers (Zhao et al., 2018; Sun et al., 2019).

Synchrotron radiation SAXS and nano-CT are two radiation methods that have high resolution. Furthermore, the pore structure detection range of the two methods is complementary. In this study, synchrotron radiation SAXS and nano-CT were combined to quantify the nano- to micro-pore structure of two bituminous coal samples. Pores between 2 nm and 70 nm in diameter were characterized by SAXS. PSD and fractal dimension features of the corresponding pores were quantified and discussed. Moreover, pores with the size from 60 nm to 2 μm were detected by nano-CT. The 3D pore structure in nanoscale was visualized and subdivided into pore and throat. The box-counting method was used to calculate the fractal dimension of the tested pores. The results of this study can provide a wider range of pore structure parameters that can help investigate CBM development.

2 Materials and methods

2.1 Descriptions of the apparatus and facilities

The synchrotron radiation SAXS and nano-CT experiments were conducted at the Beijing Synchrotron Radiation Facilities (BSRF), Beijing, China. The SAXS facilities have X-ray with a wavelength of 1.54 Å and a beam size of 20 mm and 5 mm in horizontal and vertical directions, respectively. The scattering angle varies between 0° and 5° and SAXS images are recorded by a detector (Mar 165 CCD). The nano-CT facility runs continuously from 5 to 12 keV and the size of the light source is 2.46 mm and 0.84 mm in horizontal and vertical directions, respectively. A detailed description of facilities can be found in the authors' previous studies (Zhao et al., 2014, 2018).

2.2 Sample collection and preparation

Two coal samples were collected from seam No. 11 in Xinzhouyao Mine (sample No. 1) and seam No. 9 in Tangshan Mine (sample No. 2). The petrophysical parameters of the two samples were measured and listed in Table 1 and Table 2. The values of vitrinite reflectance ($R_{o,max}$) of the samples are 0.81% and 1.12%, respectively. The inertinite group and the liptinite group of the two samples are quite similar. The vitrinite group of sample No. 1 (75.4%) is much higher than that of sample No. 2 (61.6%). The mineral matter of sample No. 1 (2.6%) is much lower than that of sample No. 2 (17.5%), especially, the clay mineral of sample No. 2 is 4.2%, but that of sample No. 1 is only 0.2%.

For SAXS experiments, coal samples were prepared into circular wafer slices with a thickness of 0.5 mm and a diameter of 9.5 mm. The prepared wafers were placed into the sample chamber. The sample chamber was composed of upper and lower plates, which were fastened by six hexagonal screws. A cavity with a 10 mm diameter was drilled into the center of the lower plate.

For nano-CT experiments, coal samples were pulverized down to fine particles, and then the particles with diameters of less than 10 μm were selected under the microscopy. The selected particle was stuck to the pin tip, and then the pin with the stuck particle was placed on the sample turntable, as shown in Fig.1(a). Finally, a particle with a diameter of 0.5 μm was stuck onto the sample under the instrument for mounting gold particle, as shown in Fig. 1(b), serving as the identification point for the subsequent image positioning.

2.3 Geological settings

Xinzhouyao Mine belongs to the Datong Coalfield, which is located in the northern part of Shanxi Province. The Datong Coalfield is a Neocathaysian platform, which is

Table 1 Results of vitrinite reflectance of coal samples

Sample number	Mine site	R_{min}/%	R_{max}/%	$R_{o,max}$/%	Classification
No. 1	No. 11 seam, Xinzhouyao Mine	0.76	0.85	0.81	High-volatile A bituminous
No. 2	No. 9 seam, Tangshan Mine	0.91	1.13	1.12	High-volatile A bituminous

Table 2 Results of maceral compositions of coal samples

Sample number	Vitrinite group/%	Inertinite group/%	Liptinite group/%	Mineral matter/%	
				Clay mineral	Non-clay mineral
No. 1	75.4	20	1.8	0.2	2.4
No. 2	61.6	19.3	1.6	4.2	13.3

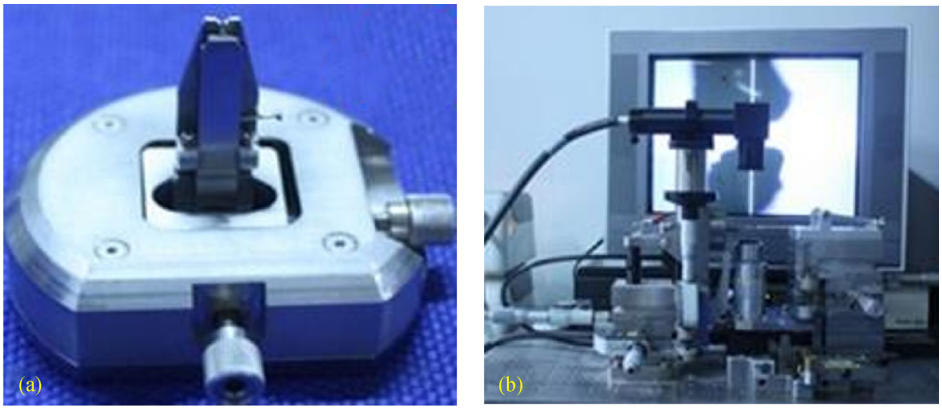

Fig. 1 Instruments used in synchrotron radiation nano-CT imaging. (a) Sample turntable with pin, (b) instrument for mounting gold particle on the sample (Sun et al., 2019).

opposite to the Cenozoic rift basin of Datong. Between the two, there is the Kouquan Mountain piedmont fault, belonging to the third uplift zone formed in the Neocathaysan period. Due to the influence of the east-west structural system, the main structural line of the Datong Coalfield is in the north-east orientation. The Datong Coalfield includes Cambrian strata, Ordovician strata, Carboniferous strata, Permian strata, Jurassic strata, Cretaceous strata, and Cenozoic strata. Affected by previous tectonic movements, some strata in the early coalfield have been eroded. Xinzhouyao Mine belongs to the Jurassic Datong Formation strata, which is composed of continental clastic rocks, coal seams, clay rocks and a small number of mixed rocks. The coal seam from which the sample was collected has a burial depth of 310–350 m, a thickness of 5.6–9.4 m, and a dip angle of 1°–10°. The immediate roof is siltstone with a thickness of 1.2–1.8 m, and the main roof is gray coarse sandstone with a thickness of 16.5–33.2 m. The coal seam consists of bright and dark bands. The texture is hard, and the fracture is generally flat and occasionally stepped, with a small number of endogenous fissures and horizontal beddings.

Tangshan Mine belongs to the Kaiping Coalfield. The Kaiping Coalfield has relatively well-developed strata. The coal measures belong to the Late Paleozoic Carboniferous-Permian coal-bearing structure. The floor of coal measures is Cambrian-Ordovician, and the upper overburden is Permian and Cenozoic. Its stratigraphic sequence is consistent with the depositional types of other parts of North China during the same period. The strata of Ordovician, Silurian, Devonian and Lower Carboniferous have been partly eroded, making the Tangshan Formation strata and the Majiagou Formation strata coincide. The upper Carboniferous-Permian is coal-bearing strata, and most of the coal-bearing strata are covered by Quaternary loess, where there are also sporadic exposures. Tangshan mine belongs to the Carboniferous Tangshan Formation strata. There are many folds in the upper part of the minefield, and the thickness of the coal strata is incomplete; however, the coal structure is stable and hard. The main roof and the immediate roof are gray fine sandstone and dark gray sandy mudstone, respectively.

2.4 Experimental procedures and image processing

The synchrotron radiation SAXS and nano-CT experimental procedures have been described in authors' previous papers in detail, available for readers' reference (Zhao et al., 2019; Zhao et al., 2018).

The SAXS images captured by the SAXS apparatus need to be transformed into data by FIT2D software. Data processing by FIT2D software package involved: 1) importing the two-dimensional images, 2) locating the coordinates of the center point of the images, 3) determining the integration area around the center point, and finally 4) exporting one-dimensional scattering data.

The recorded nano-CT images were imported into Avizo that is a commercial 3D image analysis software package. Based on the image stacking, reconstruction of 3D pore structure and quantitative analysis were conducted. Figures 2(a) and 2(d) show 3D reconstruction images of the two samples and the selection of the corresponding representative element volume (REV). According to Jiang et al. (2012), when the size of the digital core is larger than or equal to 200 nm × 200 nm × 200 nm pixels, the physical parameters of the sample pore structure are almost independent of the sample size. We chose the REV of 250 nm× 250 nm × 250 nm pixels with each pixel size of 14.59 nm × 14.59 nm × 14.59 nm and used the 3D reconstruction model of coal for quantitative analysis.

In the selected REV, there were noises on the raw gray scale images, which reduced the efficiency and accuracy of the pore structure identification. Median filter, a noise-removing method being effective in removing such noises (Gallagher and Wise, 1981), was hence applied to filter these noises in this study. Figures 2(b) and 2(e) show the images before filtration and Figs. 2(c) and 2(f) show the images after filtration.

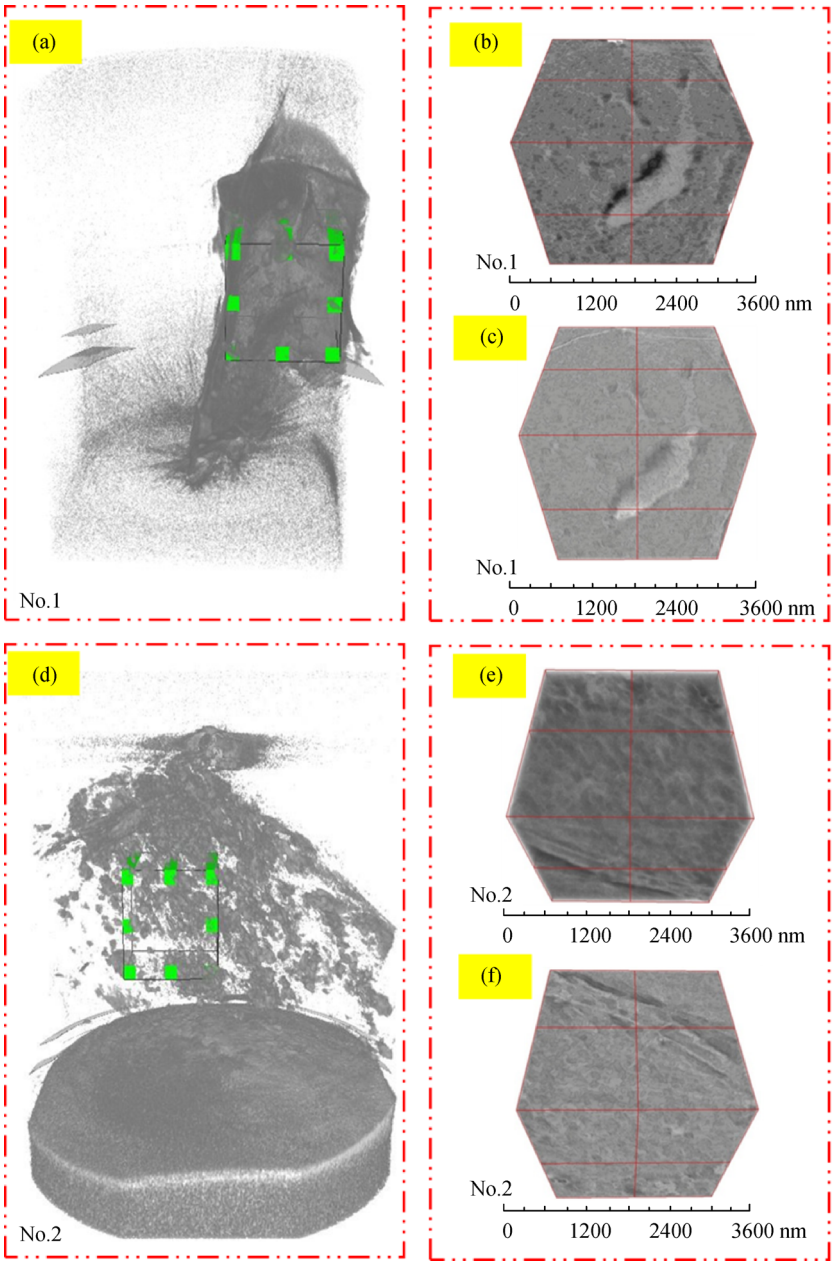

Fig. 2 Nano-CT image processing. (a) and (d) present 3D reconstruction images and REV selection, (b) and (e) present REV images before median filtration, and (c) and (f) present REV images after median filtration.

The images with noise elimination were used to extract and quantify the pore structure. The segmentation threshold was initially determined according to the distribution of the gray scale of the images, shown in Fig. 3. The distribution of the gray scale values of the images was found to be unimodal. BCVM algorithm, suitable to deal with the images with the gray values presenting unimodal distribution (Baradez et al., 2004), was selected to determine the segmentation threshold value of nano-CT images. Based on the estimated results, the pore gray scale values range between 149 and 157 for sample No. 1, and between 174 and 182 for sample No. 2. The detailed threshold estimation procedures and principles have been reported in our previous work (Zhao et al., 2018).

3 Results and discussion

3.1 Characterization of pore structure by synchrotron radiation SAXS

For SAXS experiments, Fig. 4 shows the relationship between the scattering intensity (I) and the scattering

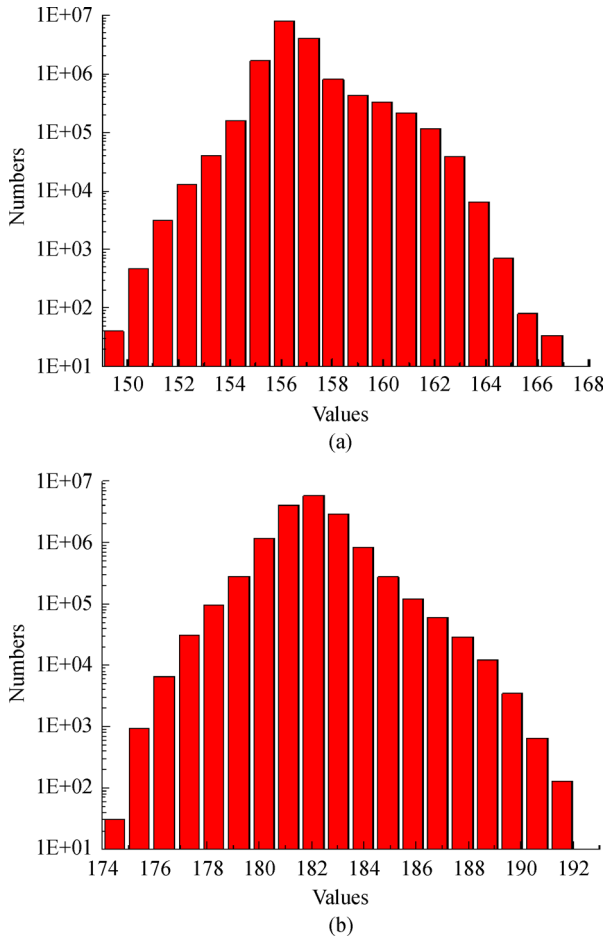

Fig. 3 Distribution of REVs' gray values. (a) No. 1-REV, (b) No. 2-REV.

vector (q). According to the range of q, the pore range of the two samples can be calculated according to the equation $D = 2\pi/q$ (Radlinski et al., 2004). D is the pore diameter (nm) and q is the scattering vector (1/nm). For sample No. 1, $0.0878 < q < 2.7671$, D can be calculated to be $2.271\ \text{nm} < D < 71.530\ \text{nm}$. For sample No. 2, $0.0872 < q < 1.7035$, thus $3.788\ \text{nm} < D < 72.055\ \text{nm}$. Therefore, the measured PSD range by SAXS in this work is approximately 2–70 nm.

Guinier law (Guinier and Fournet, 1955), Debye law (Li et al., 2000) and Porod law (Li et al., 2001) have been widely used in SAXS data analysis. Porod law reflects the variation of scattering intensity as a function of scattering vector and can be used to deal with the scattering deviation phenomenon. Guinier law primarily reflects PSD of coal and rock materials. Here, Porod law was used to calibrate and analyze the scattering data, and Guinier law was used to calculate the average gyration radius of pores in coal samples. Porod law states that under ideal long-slit light sources, the scatter has a nonuniform region of electron density and a clear interface, and when q tends to an infinite value, I follows the relationship (Li et al., 2001),

$$\lim_{q\to\infty}[q^4\cdot I(q)] = \mathrm{K} \quad \text{or} \quad \lim_{q\to\infty}\ln[q^4\cdot I(q)] = \ln\mathrm{K}, \qquad (1)$$

where, K is defined as the Porod constant, q is the scattering vector (1/nm), and $I(q)$ is the scattering intensity (a.u.).

The negative deviation of Porod law is caused by the ambiguity of the boundary in the scattering system, which means that the term on the left in Eq. (1) decreases with q increasing. When the electron density in the scattering system fluctuates, it causes the positive deviation at which the Porod curve no longer tends to be parallel and shifts upward and the slope turns into a positive value for the high q region.

Figure 5 shows the Porod curves of the two samples and their calibrations. Obviously, the Porod curves show a positive deviation. This positive deviation is due to the nonuniform region of electron density in coal samples, which caused coal samples to present the nonideal two-phase system. The premise of quantitatively counting PSD was to remove the scattering caused by the nonuniform region of electron density and calibrate the Porod curves to

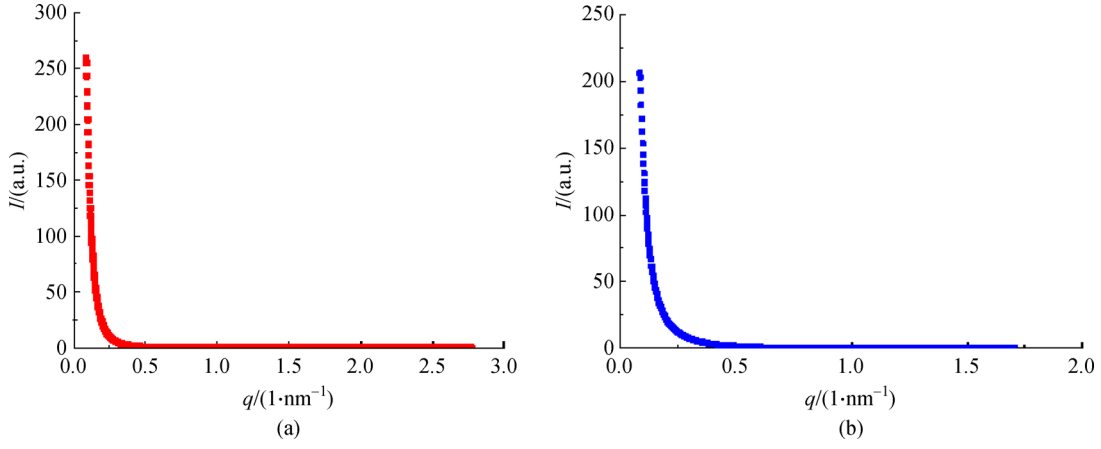

Fig. 4 Curves of scattering intensity I and scattering vector q. (a) Sample No. 1, (b) Sample No. 2.

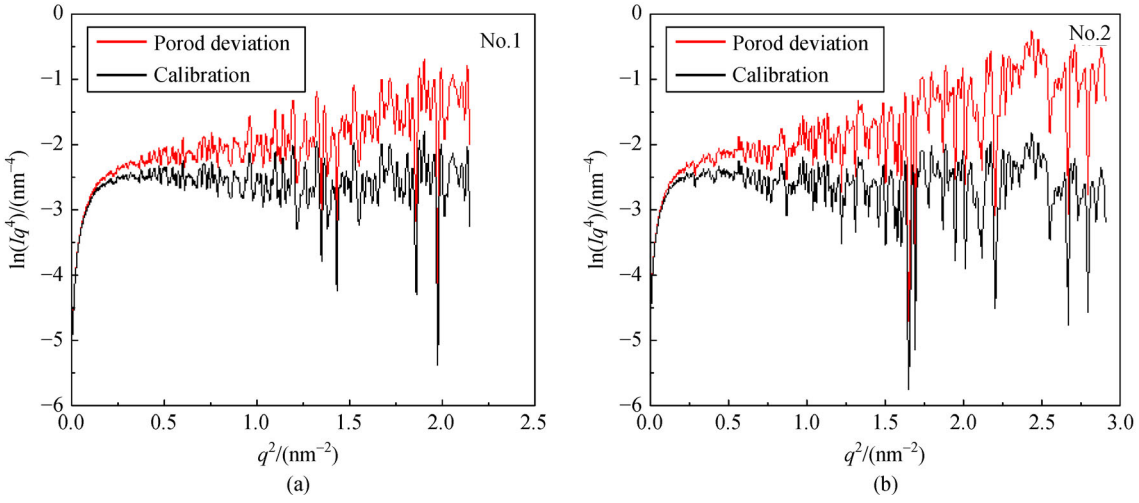

Fig. 5 Porod deviation and calibrated curves. (a) Sample No. 1, (b) Sample No. 2.

get the effective pore scattering.

An important equation for calculating the average gyration radius of pores (R_g) is Guinier equation (Guinier and Fournet, 1955). For M non-interfering pore systems, the scattering intensity can be expressed as Eq. (2) (Guinier and Fournet, 1955),

$$I(q) = I_e \cdot M \cdot n^2 \cdot \exp\left(-\frac{q^2 R_g^2}{3}\right), \quad (2)$$

where, I_e is the scattering intensity of an electron (a.u.), M is the number of pores, n is the number of electrons in a pore, R_g is the average gyration radius of pores (nm), q is the scattering vector (1/nm), and $I(q)$ is the scattering intensity (a.u.).

Figure 6 shows the Guinier scattering curves of the two samples. R_g was obtained through regression of the intensity slope in the low q region, where q^2 ranges within 0–0.1. Then, R_g values were calculated as 11.56 nm (sample No. 1) and 11.71 nm (sample No. 2).

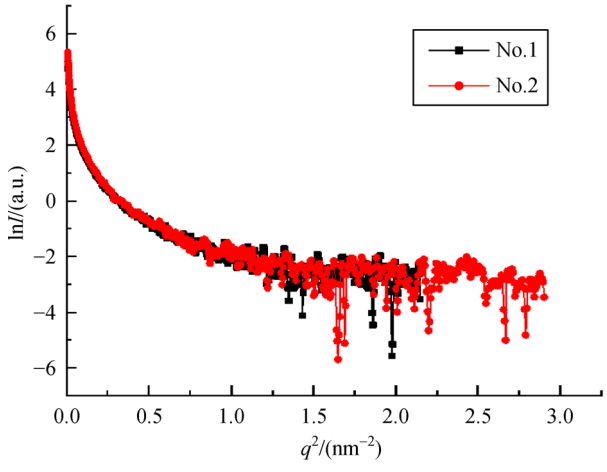

Fig. 6 Guinier curves.

The average actual radius (R) of pores is different from the average gyration radius (R_g) of pores. For SAXS theory, R_g has to be calculated first in order to obtain R. Different pore shapes correspond to different conversion relationship between R and R_g. SAXS theory in the application of coal research usually assumes that pores in coal mainly possess a sphere shape (Song et al., 2014). If the shape of pores is approximately sphere, the relationship between R and R_g can be shown as Eq. (3) (Guinier and Fournet, 1955),

$$R_g = \sqrt{\frac{3}{5}} R, \quad (3)$$

where, R_g is the average gyration radius of pores (nm), and R is the average actual radius of pores (nm).

Based on Eq. (3), the values of R were obtained with the results of 14.93 nm (sample No. 1) and 15.12 nm (sample No. 2), therefore, the average pore diameters obtained using Guinier curves are 29.86 nm and 30.24 nm, respectively.

The current statistical methods of SAXS theory include stepwise tangent method, lognormal distribution method, Shull-Ross method, and maximum entropy probability method (Jellinek et al., 1946; Roess and Shull, 1947; Potton et al., 1988; Beaucage et al., 2004). The effectiveness of the maximum entropy probability method in processing SAXS data of coal and rock has been verified in the previous study (Zhao et al., 2014), therefore, the maximum entropy probability method was used for SAXS data processing here.

Figure 7 shows the PSD curves based on SAXS. The pore diameter detected by SAXS mainly lies in the range of 2–70 nm. In this tested size range, the PSD curves of samples No. 1 and No. 2 were found to be similar and both of them present unimodal distributions. These results are

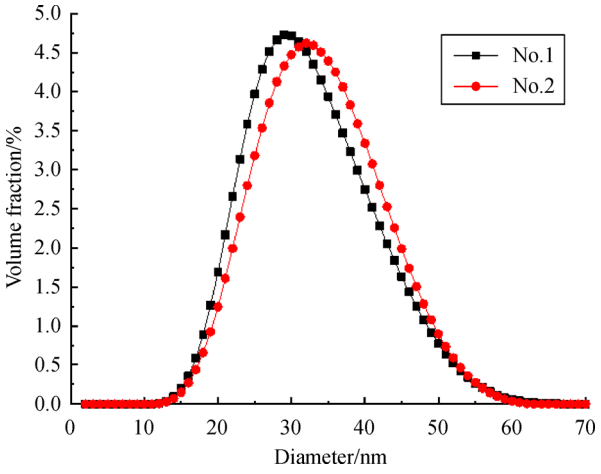

Fig. 7 PSD curves based on SAXS.

consistent with the PSD curves of tectonically deformed coals presented by Song et al. (2014). As the pore size increases, the volume fraction remains nearly zero within 2–10 nm and then it sharply increases up to the peak, and it decreases sharply until pore diameter reaches 60 nm and slowly to nearly zero within 63–70 nm. The peak of pore size of sample No. 1 appears between 25 nm and 35 nm, and that of pore size of sample No. 2 appears between 27.5 nm and 37.5 nm. The average pore diameters of the two samples are almost the same. The average pore diameter of sample No. 1 (32.08 nm) is slightly smaller than that of sample No. 2 (33.15 nm). Here, it was found that the average pore diameters (sample No. 1: 29.86 nm and sample No. 2: 30.24 nm) obtained using Guinier curves are slightly lower than those calculated by the maximum entropy probability method. The reason causing the difference needs to be further investigated.

3.2 Characterization of pore structure by synchrotron radiation nano-CT

For nano-CT experiments, after determining the segmentation threshold, we initially segmented the matrix and the pore structure, as shown in Fig. 8, and then the equivalent pore network model of REV was established to simplify the coal geometric topology and quantify the coal pore structure parameters. Figure 9 shows the equivalent network models of the two samples' REV.

Figures 9(a) and 9(h) present the pore and throat network model, which were further segmented into the pore network model shown in Figs. 9 (b) and 9(i) and the throat network model shown in Figs. 9(c) and 9(j). Figures 9(d) and 9(k) present the pore diameter statistics. The pore diameter detected by nano-CT is above 60 nm, mainly in the range of 60–2000 nm, which approximately coincides with the macropore range. Therefore, the results of nano-

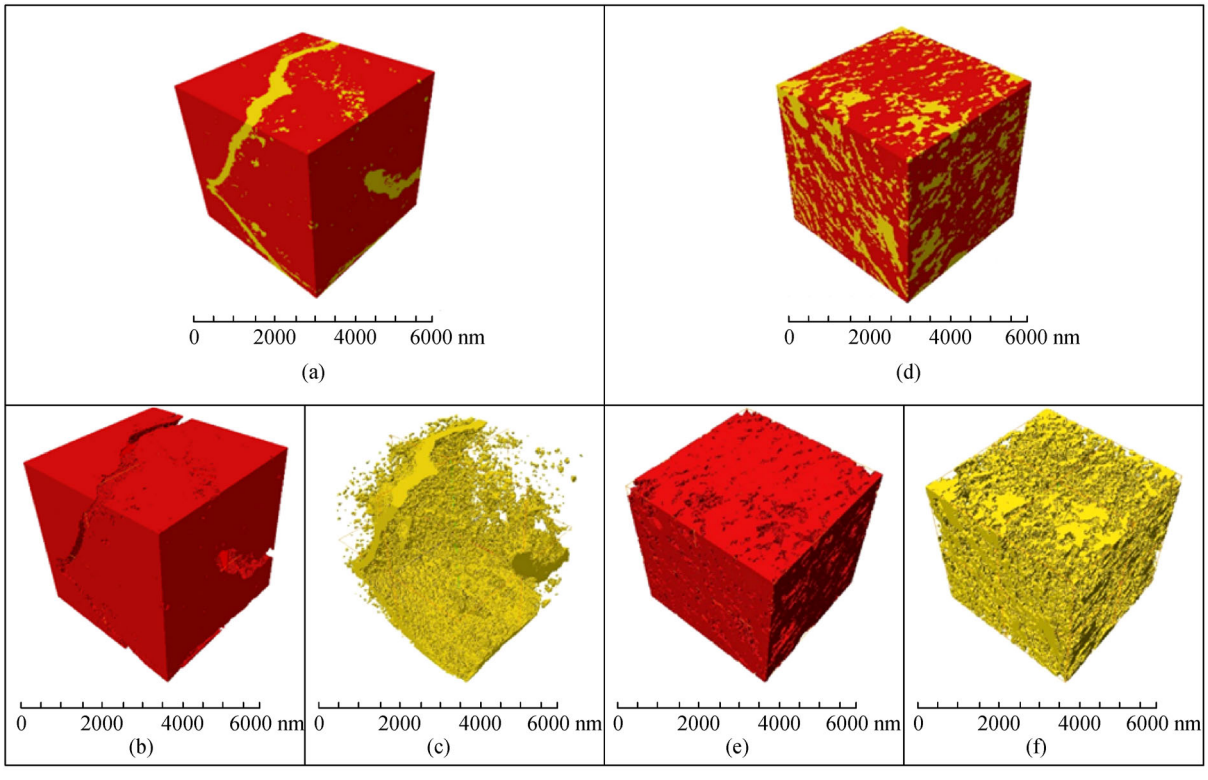

Fig. 8 Segmentation of matrix and pore structure of coal. (a) and (d) present all components of No. 1-REV and No. 2-REV, (b) and (e) present the matrix component of No. 1-REV and No. 2-REV, and (c) and (f) present the pore structure component of No. 1-REV and No. 2-REV.

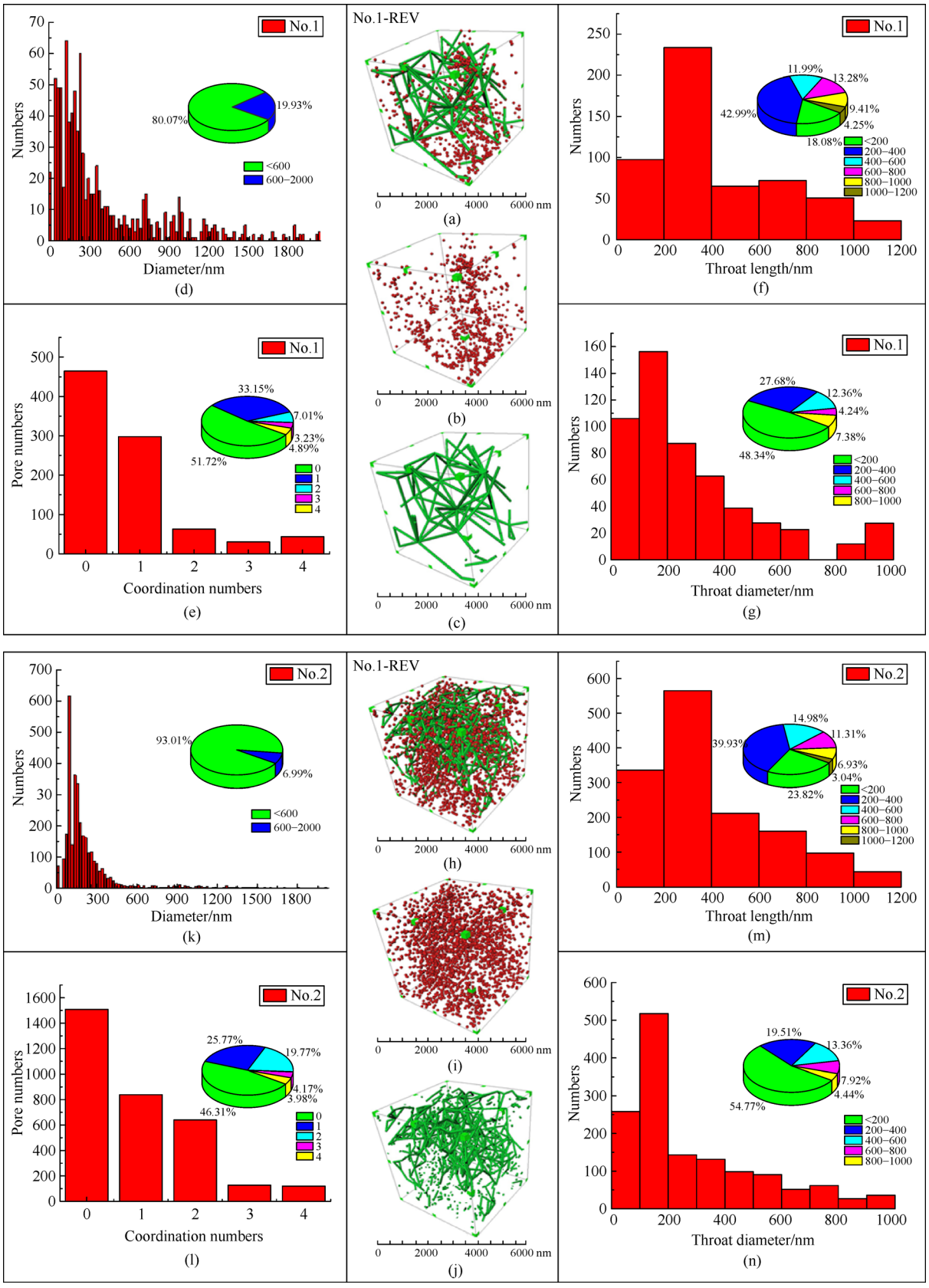

Fig. 9 The equivalent network model of coal samples' REV. (a) and (h) present the pore and throat network model, (b) and (i) present the pore network model, (c) and (j) present the throat network model, (d) and (k) present the pore diameter statistics, (e) and (l) present the pore coordination number statistics, (f) and (m) present the throat length statistics, and (g) and (n) present the throat diameter statistics.

CT can be analogously used to characterize the macropore characteristics. In the range of 60–2000 nm, the pore number of sample No. 2 (3263) is much higher than that of sample No. 1 (899). Most pores are distributed within the range of 60–600 nm, accounting for 80.07% for sample No. 1 and 93.01% for sample No. 2 of total pore numbers. The pore diameters within the 600–2000 nm range account for a relatively small portion, accounting for 19.93% for sample No. 1 and 6.99% for sample No. 2 of total pore numbers. The average pore diameter of sample No. 1 (212.67 nm) is smaller than that of sample No. 2 (255.57 nm).

The coordination number is defined as the number of a pore connected with other pores, which is an important index reflecting the pore connectivity (Zhao et al., 2018). The interconnectivity of coal pores is an important parameter for defining the fluid flow transport and storage properties. Figures 9(e) and 9(l) show the pore coordination number statistics. The authors would like to point out that this study only collects the coordination numbers ranging from 0–4 since the number of pores with the coordination numbers over 4 is less than 10. Pores with the coordination number 0 account for 51.72% and 46.31% of the total pore numbers in samples No. 1 and No. 2, respectively. This means nearly half of the total pores are closed pores. Pores with the coordination numbers ranging within 1–4 account for 48.28% and 53.69% of the total pore numbers in samples No. 1 and No. 2, respectively. Based on the results, the pore connectivity of sample No. 2 is better than that of sample No. 1. It also should be noted that the interconnectivity based on the coordination number specifically refers to whether the pore connects with its neighboring pores, considering the constraints on the nano-CT resolution. In other words, the pores appear to be isolated in nano-CT images, but they may be interconnected to the finer channels not detected.

Figures 9(f) and 9(m) present the throat length statistics. Figures 9(g) and 9(n) show the throat diameter statistics. The highest frequency of both samples' throat length appears within the 200–400 nm pore diameter range. Throats with lengths under 400 nm account for 61.07% of the total throat number in sample No. 1 and 63.75% of the total throat number in sample No. 2. The average throat length of sample No. 1 (425.68 nm) is smaller than that of sample No. 2 (485.46 nm). For the throat diameter, the highest frequency of both samples appears within the range of 0–200 nm. Throats with diameters under 200 nm account for 48.43% of the total throat number in sample No. 1 and 54.77% of the total throat number in sample No. 2. The average throat diameter of sample No. 1 (156.45 nm) is greater than that of sample No. 2 (132.38 nm).

3.3 Impact of coal components on pore structure

Based on the SAXS results, the pore structure shows a similar pattern for the tested coal samples. This may be caused by the fact that the metamorphic grades of sample No. 1 ($R_{o,max}$ = 0.81%) and sample No. 2 ($R_{o,max}$ = 1.15%) are close. The metamorphic grade of coal plays an important role in determining the pore structure because it is a comprehensive reflection of geological effects including temperature, pressure, and time (Coutinho et al., 2007).

However, it should be noted that the pore numbers within the 60–2000 nm pore diameter range (sample No. 1: 899 and sample No. 2: 3263) show evident differences. The factors causing these differences were investigated from the perspective of coal components. Based on the perspective of physical properties, the higher the mineral matter content is, the harder the coal is. Therefore, the pore structure is less affected by sedimentary compaction due to robust structure (Zhang et al., 2008). It was found that the mineral matter content of sample No. 1 (2.6%) is much lower than that of sample No. 2 (17.5%). Consequently, compared with sample No. 1, the pore structure of sample No. 2 with higher mineral matter content may be less affected by sedimentary compaction. Meanwhile, from the viewpoint of the hydrocarbon generation from organic matter, the catalysis effect of clay mineral can also significantly enhance the generation of displacing hydrocarbon pores. The higher the clay mineral content is, the more pores are generated by the catalysis effect of clay mineral (Zhang et al., 2008). It was found that the clay mineral content of sample No. 2 is 4.2%, whereas that of sample No. 1 is only 0.2%. Therefore, compared with sample No. 1, there are more pores generated by the catalysis effect of clay mineral in sample No. 2. These are two factors causing sample No. 2 to manifest a much higher number of pores than sample No. 1 does.

3.4 Fractal dimensions by synchrotron radiation SAXS and nano-CT

For an object with fractal features, its SAXS intensity can be represented by a power law (Zhang et al., 2017),

$$I(q) = I_0 q^{-\alpha}, \tag{4}$$

where, α is the fractal parameter with the values ranging between 0 and 4.

Taking the natural logarithm on both sides of Eq.(4), the slope of the linear region of the $\ln I(q) - \ln q$ curve is defined as d, make $\alpha = -d$. When α varies between 3 and 4, the scatter shows surface fractal feature and the value of surface fractal dimension (D_s) is $D_s = 6 - \alpha$. When α varies between 0 and 3, the scatter shows mass fractal feature and the value of mass fractal dimension (D_m) is $D_m = \alpha$ (Reich et al., 1992; Nakagawa et al., 2000).

Figure 10 shows the fractal curves based on SAXS results. The fractal dimension was obtained by making a tangent to the double logarithmic curve within different $\ln q$ ranges. Different $\ln q$ ranges have different fractal para-

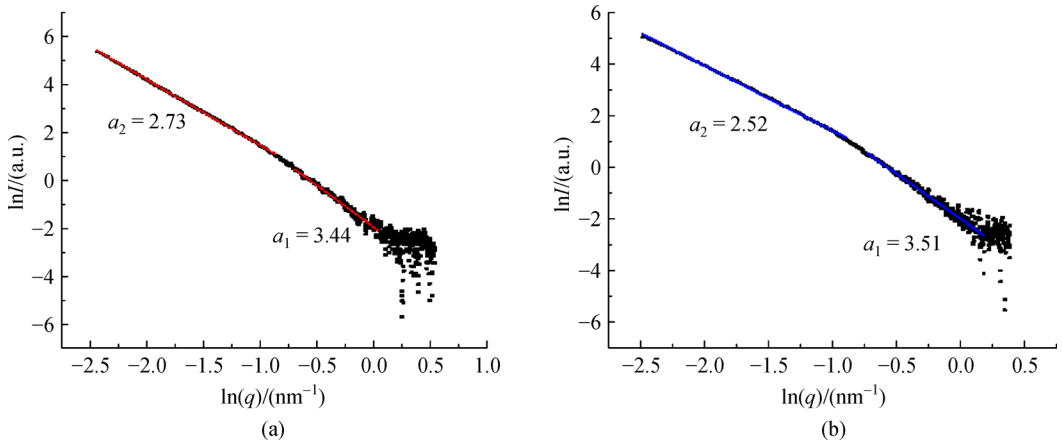

Fig. 10 Double logarithmic curves of scattering intensity I and scattering vector q. (a) Sample No. 1, (b) Sample No. 2.

meters. As can be seen in Table 3, for sample No. 1, its fractal parameter within the range of −0.70–0.04 is α_1 = 3.44, indicating a surface fractal feature with D_s = 2.56. For the range of −2.44––0.85, α_2 is 2.73, suggesting that it shows a mass fractal feature with the value of D_m = 2.73. For sample No. 2, its fractal parameter within the range of −0.72–0.17 is α_1= 3.51, indicating that it shows a surface fractal with the value of D_s = 2.49. For the range of −2.48–−0.89, α_2 is 2.52, suggesting that it shows a mass fractal behavior with the value of D_m = 2.52.

The box-counting method has been widely applied to measure the fractal dimension of the porous medium due to its easy implementation and applicability to objects with or without self-similarity (Xie, 1993; Babadagli and Develi, 2003). For nano-CT image analysis, here the box-counting method was adopted to calculate the 2D and 3D fractal dimensions, based on the workflow suggested by Zhao et al. (2017) as follows:

Use a box with a length δ to cover a sample with dimension D (the dimension of the box is the same as the dimension of the sample). The number of boxes completely covering the sample is recorded as $N(\delta)$. The following relationship exists between the number of boxes and the box length (Wang et al., 2012),

$$D = \lim_{\delta \to 0} \frac{\log N(\delta)}{-\log \delta}, \tag{5}$$

where, D is the fractal dimension, δ is the box length, and $N(\delta)$ is the number of boxes.

Taking the natural logarithm of both sides of Eq. (5), it gives,

$$\ln N(\delta) = \mathrm{C} + D\ln(1/\delta), \tag{6}$$

where, C is a constant.

Drawing a logarithmic curve of ln$N(\delta)$–ln$(1/\delta)$ based on Eq. (6) and obtaining the absolute slope value of ln$N(\delta)$–ln$(1/\delta)$ yield the value of the fractal dimension.

Figure 11 shows the 2D fractal dimension (D_{2D}) of different slices in the two samples. The curves show a variation with the slice number. The slice number was directly determined by the location of the scan. This variation indicates that different scan positions have different fractal features. As can be seen in Table 3, the average D_{2D} values of No. 1-REV and No. 2-REV are 1.516 and 1.346, and the minimum and maximum D_{2D} values of No. 1-REV are 1.469 (slice 68) and 1.533 (slice 153). The values of D_{2D} for No. 2-REV are 1.264 (slice 180) and 1.427 (slice 118). The values of 3D fractal dimension (D_{3D}) of No. 1-REV and No. 2-REV are 2.538 and 2.351.

For SAXS fractal theory, D_s represents the irregularity of pore surface. The larger D_s denotes higher irregularity of pore surface. D_m represents the heterogeneity of pore structure and larger values of D_m denote higher heterogeneity of pore structure. It can be seen from Table 3 that within the range of mesopores, the surface and mass fractal dimensions of sample No. 1 (D_s = 2.56, D_m = 2.73) are found to be greater than those of sample No. 2 (D_s = 2.49, D_m = 2.52). This can be interpreted by the fact that the irregularity of pore surface and the heterogeneity of pore structure of sample No. 1 are greater than those of sample No. 2.

Table 3 Results of fractal dimensions of two samples based on SAXS and nano-CT

Sample	SAXS (2–70 nm)				nano-CT (60–2000 nm)	
	α_1	D_s	α_2	D_m	D_{2D}	D_{3D}
No. 1	3.44	2.56	2.73	2.73	1.469–1.553	2.538
No. 2	3.51	2.49	2.52	2.52	1.264–1.427	2.351

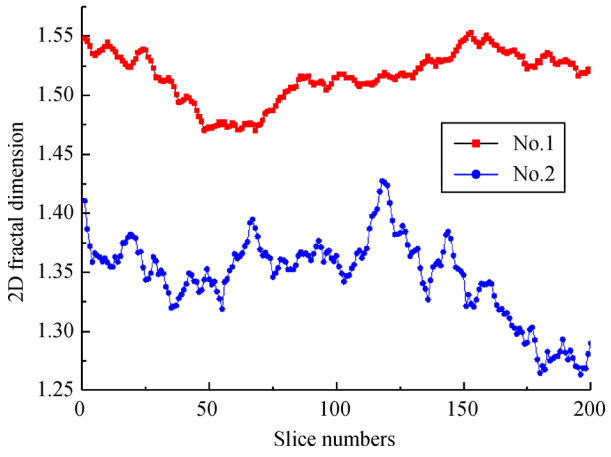

Fig. 11 2D fractal dimension of coal samples.

For the box-counting method, D_{2D} represents the irregularity of the pore surface, and the larger D_{2D} values indicate higher irregularity of pore surface. D_{3D} represents the heterogeneity of the pore structure, and the larger D_{3D} values indicate the more heterogeneous pore structure. As shown in Table 3, within the range of macropores, the D_{2D} range of No. 1-REV is 1.469–1.553 which is greater than that of No. 2-REV (1.264–1.427). The D_{3D} value of No. 1-REV is 2.538 which is larger than that of No. 2-REV (2.351), which indicates that the irregularity of the pore surface and the heterogeneity of the pore structure of sample No. 1 are larger than those of sample No. 2.

Based on both SAXS and nano-CT results, it is evident that sample No. 1 has more complex pore structures, which were confirmed by the fractal dimensions. This can be used to guide future coal gas drainage design and coal utilization. Assuming the other gas transport properties including fracture/cleat permeability and desorption potential are similar, sample No. 1 will have a challenging issue for coal gas drainage because gas diffusion will be smaller than that in sample No. 2. This can be attributed to longer diffusive path and higher degree of tortuosity. This inference can be intuitively confirmed by Fig. 12.

To analyze the surface irregularity of pores in nano-CT images, the slices with the minimum and maximum D_{2D} values (black regions are pores, and white regions are matrix skeleton) are selected. The comparison results are shown in Fig. 12. The slices with the minimum and maximum D_{2D} values of No. 1-REV were labeled as S1 and S2, and those of No. 2-REV were labeled as S3 and S4. Obviously, the pore size of S2 is smaller, nevertheless, the pore surface of S2 is much rougher than that of S1, S3 and S4. Also, S3 has a relatively larger pore size and smoother pore surface. The irregularity degree of pore surface follows $S2 > S1 > S4 > S3$, which corresponds to the order of the estimated D_{2D} values of four slices.

The relative standard deviation of each sub-blocks' porosity in REV can be used to quantitatively characterize

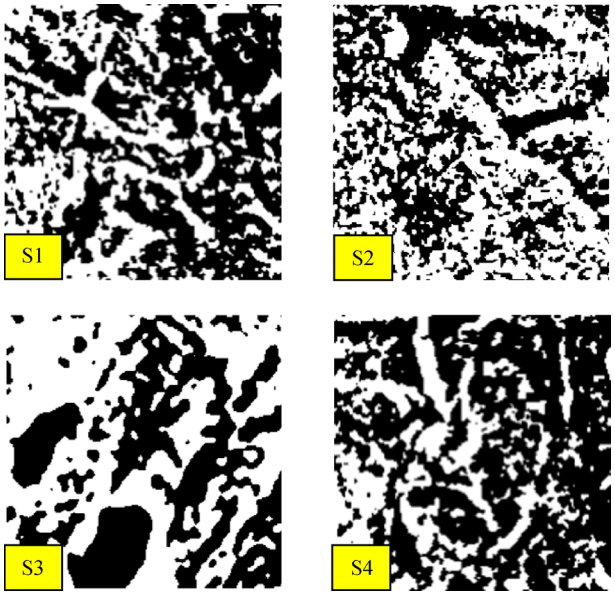

Fig. 12 Slices with minimum and maximum 2D fractal dimensions in two samples' REV. S1-Slice with the minimum D_{2D} value of No. 1-REV, S2-Slice with the maximum D_{2D} value of No. 1-REV, S3-Slice with the minimum D_{2D} value of No. 2-REV, and S4-Slice with the maximum D_{2D} value of No. 2-REV.

the pore structure heterogeneity of coals. The heterogeneity value of pore structure can be calculated by Eq. (7) (Sun, 2018b),

$$HV = \lim_{x\to\infty} \frac{\mathrm{A}\cdot x}{1+\mathrm{B}\cdot x} = \frac{\mathrm{A}}{\mathrm{B}}, \tag{7}$$

where, HV is the heterogeneity value, x is the equal-segment number of REV in the X, Y, Z directions, and A and B are fitting constants.

Figure 13 shows the regression results of the estimated heterogeneity value. The HV value of sample No. 1 (3.21)

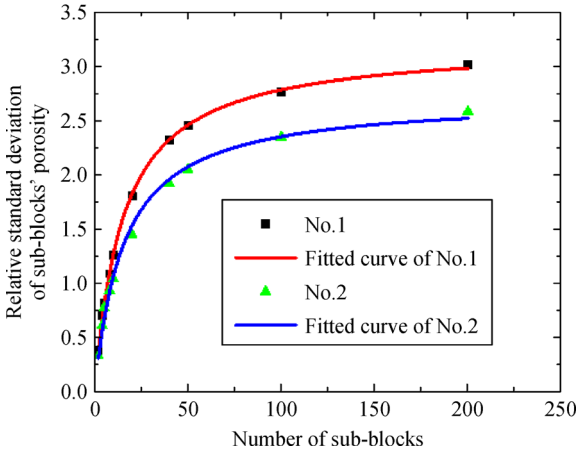

Fig. 13 The relationship between the relative standard deviation of sub-blocks' porosity and the number of sub-blocks (Sun, 2018b).

is larger than that of sample No. 2 (2.71). Physically, it proves that the pore structure of sample No. 1 is more heterogeneous than that of sample No. 2, which is consistent with the results characterized by the 3D fractal dimension. Based on the limited number of samples, this consistency verifies the effectiveness of both characterization techniques that can be chosen for the coal pore structure heterogeneity analysis. However, larger databases with different ranks and types of coal are recommended for future tests and cross-validation of this finding.

The difference in the pore surface irregularity can be attributed to the effect of mineral inclusions. The mineral inclusions widely exist in coals, which can weaken the roughness of mesopores and macropores (Li et al., 2018). In this study, the mineral content of sample No. 2 is higher than that of sample No. 1. This may be one of the factors that explain smoother surface of sample No. 2.

Li (2018) used the LPGA method to characterize the structure heterogeneity of the pores with diameters ranging 1–100 nm and the MIP method to characterize the structure heterogeneity of the pores with diameters exceeding 100 nm. Li (2018) stated that vitrinite-rich coal has more 1–100 nm diameter pores, which aggravates the pore structure heterogeneity. Combined with the fact that the vitrinite content of sample No. 1 is higher than that of sample No. 2, as observed in this work, there are likely more 1–100 nm diameter pores in sample No. 1 leading to the enhancement of its pore structure heterogeneity, as shown in Fig. 12.

4 Summary and conclusions

Considering the complementarity of synchrotron radiation SAXS and nano-CT in covering a wide range of pore structure detection, the mesopore-macropore structure of two bituminous coal samples was characterized using the two methods. Based on the experimental results, the following conclusions can be made,

1) For SAXS experiments, the pore size within the range of 2–70 nm was probed and characterized. These results covered a full range of mesopores. In mesopores, the PSD curves exhibit unimodal distribution and the average pore diameters are similar due to the affinity of metamorphic grades of the two samples.

2) The range of pore size detected by nano-CT is 60–2000 nm representing the pore characteristics of the macropores. In macropores, the sample with higher mineral matter content, especially clay mineral content, has a much higher number of pores due to being less affected by sedimentary compaction and also has more pores generated by the catalysis effect of clay mineral.

3) The fractal dimensions estimated by both methods for different pore sizes show the consistency that sample No. 1 has a more complex pore structure within the full tested range. The fractal dimension obtained by SAXS includes the surface fractal dimension representing the pore surface irregularity with the values of 2.56 and 2.49 and the mass fractal dimension representing the pore structure heterogeneity with the values of 2.73 and 2.52. The fractal dimension obtained by nano-CT includes the 2D fractal dimension representing the pore surface irregularity with the values ranging within 1.469–1.553 and 1.264–1.427; and the 3D fractal dimension representing the pore structure heterogeneity with the values of 2.538 and 2.351.

Acknowledgements The research is financially sponsored by the National Natural Science Foundation of China (Grant Nos. U1910206, 51861145403, 51874312, 52004293), China Postdoctoral Science Foundation (No. 2018M641526), Yue Qi Distinguished Scholar Project of China University of Mining & Technology (Beijing), Fundamental Research Funds for the Central Universities, Fund of China Scholarship Council and the Open Project Program of Key Laboratory of Deep Earth Science and Engineering (Sichuan University), Ministry of Education (No. DESE 202004). Zhihong Li, Guang Mo and Wanxia Huang of Beijing Synchrotron Radiation Laboratory (BSRF) are thanked for providing the SAXS and Nano-CT experimental facilities and their suggestions in conducting experiments and data processing.

References

Bale H D, Schmidt P W (1984). Small-angle X-ray-scattering investigation of submicroscopic porosity with fractal properties. Phys Rev Lett, 53(6): 596–599

Baradez M O, Mcguckin C P, Forraz N, Pettengell R, Hoppe A (2004). Robust and automated unimodal histogram thresholding and potential applications. Pattern Recognit, 37(6): 1131–1148

Beaucage G, Kammler H K, Pratsinis S E (2004). Particle size distributions from small-angle scattering using global scattering functions. J Appl Cryst, 37(4): 523–535

Benedetti A, Ciccariello S (1996). Coal rank and shape of the small-angle X-ray intensity. J Phys III, 6(11): 1479–1487

Coutinho J, Kräutner H, Sassi F, Schmid R, Sen S (2007). Recommendations by the IUGS subcommission on the systematics of metamorphic rocks: Web version 01.02.07, 16–23

Gallagher N, Wise G (1981). A theoretical analysis of the properties of median filters. IEEE Trans Acoust, 29(6): 1136–1141

Giffin S, Littke R, Klaver J, Urai J L (2013). Application of BIB-SEM technology to characterize macropore morphology in coal. Int J Coal Geol, 114: 85–95

Guinier A, Fournet G (1955). Small-angle Scattering of X-rays. Hoboken: Wiley

Jellinek M H, Soloman E, Fankuchen I (1946). Measurement and analysis of small-angle X-Ray scattering. Ind Eng Chem Anal Ed, 18 (3): 172–175

Jiang L M, Sun J M, Liu X F, Wang H T (2012). Numerical study of the effect of natural gas saturation of the reservoir rock's elastic parameters. Well Logging Technol, 36: 239–243 (in Chinese)

Li P P, Zhang X D, Zhang S (2018). Structures and fractal characteristics of pores in low volatile bituminous deformed coals by low-temperature N_2 adsorption after different solvents treatments. Fuel,

224: 661–675

Luo L, Liu J X, Zhang Y C, Zhang H, Ma J F, You Y L, Jiang X M (2016). Application of small angle X-ray scattering in evaluation of pore structure of superfine pulverized coal/char. Fuel, 185: 190–198

Li Z H, Gong Y J, Wu D, Sun Y H, Wang J, Liu Y, Dong B Z (2001). A negative deviation from Porod's law in SAXS of organo-MSU-X. Microporous Mesoporous Mater, 46(1): 75–80

Li Z H, Sun J H, Wu D, Sun Y H, Liu Y, Sheng W J, Dong B Z (2000). Determination of specific surfaces of silica xerogets by SAXS. Chin Sci Bull, 45(15): 1386–1390

Li Z T (2018). Evolution of pore-fractures of coal reservoir and its impact on CBM microcosmic flow. Dissertation for the Doctoral Degree. Beijing: China University of Geosciences (in Chinese)

Li Z T, Liu D M, Cai Y D, Ranjith P G, Yao Y B (2017). Multi-scale quantitative characterization of 3-D pore-fracture networks in bituminous and anthracite coals using FIB-SEM tomography and X-ray μ-CT. Fuel, 209: 43–53

Mahamud M, Novo M (2008). The use of fractal analysis in the textural characterization of coals. Fuel, 87(2): 222–231

Mares T E, Radliński A P, Moore T A, Cookson D, Thiyagarajan P, Ilavsky J, Klepp J (2009). Assessing the potential for CO_2 adsorption in a subbituminous coal, Huntly Coalfield, New Zealand, using small angle scattering techniques. Int J Coal Geol, 77(1–2): 54–68

Mastalerz M, He L, Melnichenko Y B, Rupp J A (2012). Porosity of coal and shale: insights from gas adsorption and SANS/USANS techniques. Energy Fuels, 26(8): 5109–5120

Nakagawa T, Komaki I, Sakawa M, Nishikawa K (2000). Small angle X-ray scattering study on change of fractal property of Witbank coal with heat treatment. Fuel, 79(11): 1341–1346

Pan J N, Niu Q H, Wang K, Shi X H, Li M (2016). The closed pores of tectonically deformed coal studied by small-angle X-ray scattering and liquid nitrogen adsorption. Micropor Mesopor Mater, 224: 245–252

Potton J A, Daniell G J, Rainford B D (1988). A new method for the determination of particle size distributions from small-angle neutron scattering measurements. J Appl Cryst, 21(6): 891–897

Radlinski A P, Mastalerz M, Hinde A L, Hainbuchner M, Rauch H, Baron M, Lin J S, Fan L, Thiyagarajan P (2004). Application of SAXS and SANS in evaluation of porosity, pore size distribution and surface area of coal. Int J Coal Geol, 59(3-4): 245–271

Reich M H, Snook I K, Wagenfeld H K (1992). A fractal interpretation of the effect of drying on the pore structure of Victorian brown coal. Fuel, 71(6): 669–672

Rodrigues C F, Lemos de Sousa M J (2002). The measurement of coal porosity with different gases. Int J Coal Geol, 48(3-4): 245–251

Roess L C, Shull C G (1947). X-Ray scattering at small angles by finely-divided solids. Part II: exact theory for random distributions of spheroidal particles. J Appl Phys, 18(3): 308–313

Rootare H M, Prenzlow C F (1967). Surface areas from mercury porosimeter measurements. J Phys Chem, 71(8): 2733–2736

Rouquerol J K K, Avnir D, Fairbridge C W, Everett D H, Haynes J M, Pernicone N, Ramsay J D F, Sing K S W, Unger K K (1994). Recommendations for the characterization of porous solids (Technical Report). Pure Appl Chem, 66(8): 1739–1758

Song X X, Tang Y G, Li W, Ceng F G, Xiang J H (2014). Pore structure in tectonically deformed coals by small angle X-ray scattering. J China Coal Soc, 39: 719–724 (in Chinese)

Suggate R P, Dickinson W W (2004). Carbon NMR of coals: the effects of coal type and rank. Int J Coal Geol, 57(1): 1–22

Sun Y F, Zhao Y X, Wang X, Peng L, Sun Q (2019). Synchrotron radiation facility-based quantitative evaluation of pore structure heterogeneity and anisotropy in coal. Pet Explor Dev, 46(6): 1195–1205

Sun Y F, Zhao Y X, Yuan L (2018a). Quantifying nano-pore heterogeneity and anisotropy in gas shale by synchrotron radiation nano-CT. Micropor Mesopor Mater, 258: 8–16

Sun Y F (2018b). Investigation of gas adsorption and diffusion behavior based on three-dimensional pore structure of coal. Dissertation for the Doctoral Degree. Beijing: China University of Mining and Technology (in Chinese)

Syed R, Sen D, Mani Krishna K V, Ghosh S K (2018). Fabrication of highly ordered nanoporous alumina membranes: probing micro-structures by SAXS, FESEM and AFM. Microporous Mesoporous Mater, 264: 13–21

Wang H, Liu Y, Song Y, Zhao Y, Zhao J (2012). Fractal dimension analysis on pore structure of artificial cores using magnetic resonance imaging. In: 2nd International Conference on Consumer Electronics, Communications and Networks, 2593–2596

Wang Y, Wang L H, Wang J Q, Zheng J G, Wang C C, Fu Y A, Song Y F, Wang Y F, Liu D Z, Jin C (2019). Multiscale characterization of three-dimensional pore structures in a shale gas reservoir: a case study of the Longmaxi shale in Sichuan basin, China. J Nat Gas Sci Eng, 66: 207–216

Xie H P (1993). Fractals in Rock Mechanics. Boca Raton: CRC Press

Zhang R, Liu S, Wang Y (2017). Fractal evolution under in situ pressure and sorption conditions for coal and shale. Sci Rep, 7(1): 8971

Zhang S H, Tang D Z, Tang S H, Xu H, Lin W J, Zhang B (2008). The characters of coal beds micropores and its influence factors in the eastern margin of Ordos Basin. Acta Geol Sin, 82: 1341–1349 (in Chinese)

Zhao Y X, Liu S M, Elsworth D, Jiang Y D, Zhu J (2014). Pore structure characterization of coal by synchrotron small-angle X-ray scattering and transmission electron microscopy. Energy Fuels, 28(6): 3704–3711

Zhao Y X, Peng L, Liu S M, Cao B, Sun Y F, Hou B F (2019). Pore structure characterization of shales using synchrotron SAXS and NMR cryoporometry. Mar Pet Geol, 102: 116–125

Zhao Y X, Sun Y F, Liu S M, Chen Z W, Yuan L (2018). Pore structure characterization of coal by synchrotron radiation nano-CT. Fuel, 215: 102–110

Zhao Y X, Zhu G P, Dong Y H, Danesh N N, Chen Z W, Zhang T (2017). Comparison of low-field NMR and microfocus X-ray computed tomography in fractal characterization of pores in artificial cores. Fuel, 210: 217–226

Zheng S J, Yao Y B, Liu D M, Cai Y D, Liu Y (2018). Characterizations of full-scale pore size distribution, porosity and permeability of coals: a novel methodology by nuclear magnetic resonance and fractal analysis theory. Int J Coal Geol, 196: 148–158